Journal of the Taiwan Institute of Chemical Engineers 78 (2017) 157–167

Contents lists available at ScienceDirect

Journal of the Taiwan Institute of Chemical Engineers

journal homepage: www.elsevier.com/locate/jtice

Synthesis and characterization of $Bi_4Si_3O_{12}$, Bi_2SiO_5, and $Bi_{12}SiO_{20}$ by controlled hydrothermal method and their photocatalytic activity

Chiing-Chang Chen[a,*], Chin-Tsung Yang[a], Wen-Hsin Chung[b], Jia-Lin Chang[a], Wan-Yu Lin[b]

[a] Department of Science Education and Application, National Taichung University of Education, Taichung 403, Taiwan
[b] Department of Plant Pathology, National Chung Hsing University, Taichung 402, Taiwan

ARTICLE INFO

Article history:
Received 3 October 2016
Revised 18 May 2017
Accepted 18 May 2017
Available online 7 June 2017

Keywords:
Bi_2SiO_5
$Bi_4Si_3O_{12}$
$Bi_{12}SiO_{20}$
Photocatalytic
Crystal violet

ABSTRACT

This is the first report that three compounds, $Bi_4Si_3O_{12}$, Bi_2SiO_5, and $Bi_{12}SiO_{20}$, can be selectively synthesized by a controlled and template-free hydrothermal method. Crystalline $Bi_4Si_3O_{12}$, Bi_2SiO_5, and $Bi_{12}SiO_{20}$ are prepared from the reaction of Na_2SiO_3 and $Bi(NO_3)_3 \bullet 5H_2O$ in an alkaline aqueous solution at 150 °C–250 °C for 24 h, whereas conventional syntheses necessitate operational temperatures above 650 °C. The composition and morphology of bismuth silicates could be controlled by adjusting some growth parameters, including reaction pH and temperature. The products are characterized by X-ray diffraction scanning electron microscope–energy–dispersive X-ray spectroscopy, high-resolution transmission electron microscopy, Diffuse Reflectance UV–visible spectroscopy, Brunauer–Emmett–Teller, and high-resolution X-ray photoelectron spectroscopy. The UV–Vis spectra demonstrate that the three materials are indirect semiconductors with optical bandgaps of 2.65, 3.30, and 3.44 eV for $Bi_{12}SiO_{20}$, Bi_2SiO_5, and $Bi_4Si_3O_{12}$, respectively. The photocatalytic efficiency of the powder suspension is evaluated by measuring the crystal violet concentration under visible-light irradiation. The order of rate constants shows $Bi_2SiO_5 > Bi_4Si_3O_{12} > Bi_{12}SiO_{20}$.

© 2017 Taiwan Institute of Chemical Engineers. Published by Elsevier B.V. All rights reserved.

1. Introduction

During the last decade, heterogeneous photocatalysis methods for environmental remediation and solar energy conversion have aroused extensive interest because they require mild reaction conditions, produce no secondary pollutants, and are inexpensive and environmentally sturdy [1]. To utilize visible light and harvest solar energy efficiently, intensive efforts have been made to develop visible-light-driven photocatalysts.

In efforts to exploit novel photocatalyst systems working under visible light, it has been revealed that orbitals of some p-block metals with a d^{10} configuration, such as Ag 4d in Ag(I), Sn 5 s in Sn(II) and Bi 6 s in Bi(III), could hybridize O 2p levels to form a new preferable hybridized valence band (VB), thus narrowing the band gap to harvest visible light. In terms of low toxicity and earth abundance, bismuth-based materials are more appropriate candidates; on the other hand, bismuth based semiconductors have shown efficient photocatalytic performance in waste water purification and harmful pollutant removal. Hence, considerable attention has been drawn to bismuth-based semiconductors, which could be endowed with strong visible light absorption and excellent photocatalytic activity [2–5].

Recently, Bi-based layered structure compounds, within the Aurivillius family, such as BiOX (X = Cl, Br, I) [2,3], $Bi_4Ti_3O_{12}$ [6], Bi_2WO_6 [7], $BiVO_4$ [8], Bi_3TiNbO_9 [9], Bi_7VO_{13} [4], $Bi_{11}VO_{19}$ [5], etc., have been extensively researched as highly efficient photocatalysts because of their unique layered structures and highly catalytic activities. It is thought that the Bi 6 s and O 2p levels can make a greatly dispersed hybridized valence band, which would favor the mobility of photogenerated holes and the oxidation reaction, inducing efficient separation of photogenerated electron-hole pairs and improving photocatalytic efficiency [10].

The Bi_2O_3-SiO_2 binary system [11–14] consists of three compounds of $Bi_{12}SiO_{20}$, $Bi_4Si_3O_{12}$, and Bi_2SiO_5. Bi_2O_3 and SiO_2 form silicates (such as $Bi_2Si_3O_9$, $Bi_4Si_3O_{12}$, Bi_2SiO_5, and $Bi_{12}SiO_{20}$) presents different molar ratios. Among these, the compounds $Bi_4Si_3O_{12}$ and $Bi_{12}SiO_{20}$ have several interesting properties such as a large value of the dielectric constant, piezoelectric and elasto-optic coefficients, and high refractive index; hence they are technologically crucial [15–19]. Bi_2SiO_5, a substance of the Aurivillius family is a promising material with relatively good dielectric and piezoelectric properties and nonlinear optical effects. Its luminescent properties were also reported in a recent study by Duan et al., who synthesized Bi_2SiO_5 by using hydrothermal methods, which demonstrated excellent photocatalytic abilities

* Corresponding author.
E-mail addresses: ccchen@mail.ntcu.edu.tw, ccchen@ms3.ntcu.edu.tw (C.-C. Chen).

http://dx.doi.org/10.1016/j.jtice.2017.05.021
1876-1070/© 2017 Taiwan Institute of Chemical Engineers. Published by Elsevier B.V. All rights reserved.

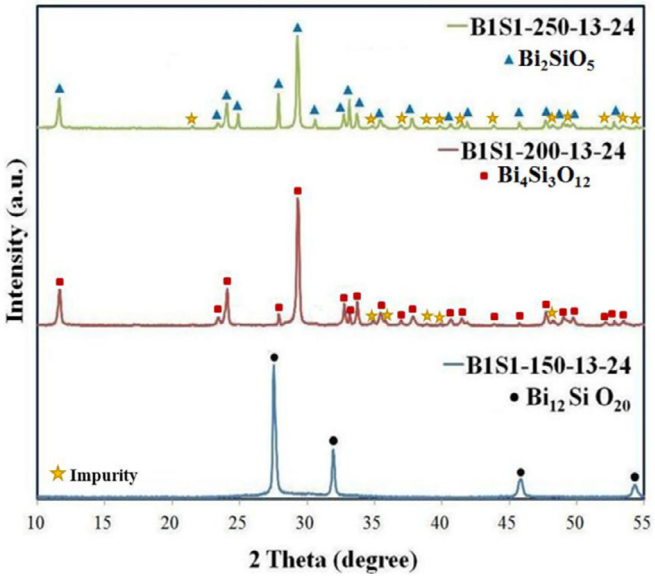

Fig. 1. XRD patterns of the as-prepared Bi_2SiO_5, $Bi_4Si_3O_{12}$, and $Bi_{12}SiO_{20}$ samples under different temperatures, pH = 13, and Molar ratio (Bi/Si) = 1/1.

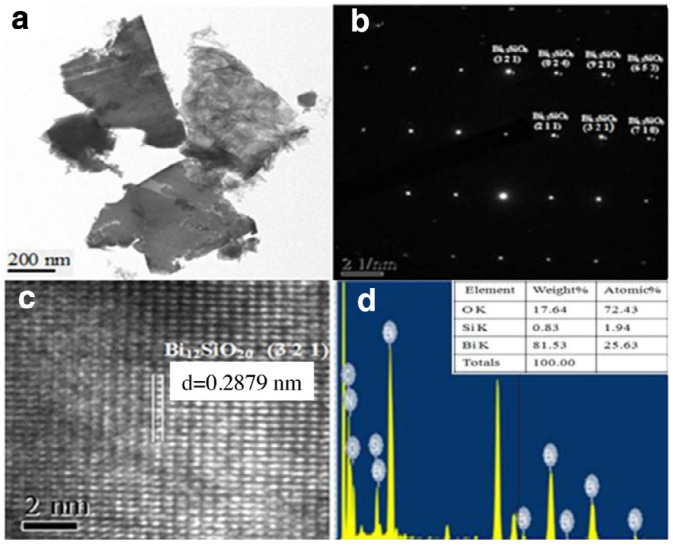

Fig. 2. (a) FE-TEM images, (b) SAED, (c) HRTEM images, and (d) EDS of $Bi_{12}SiO_{20}$ prepared by the hydrothermal autoclave method.

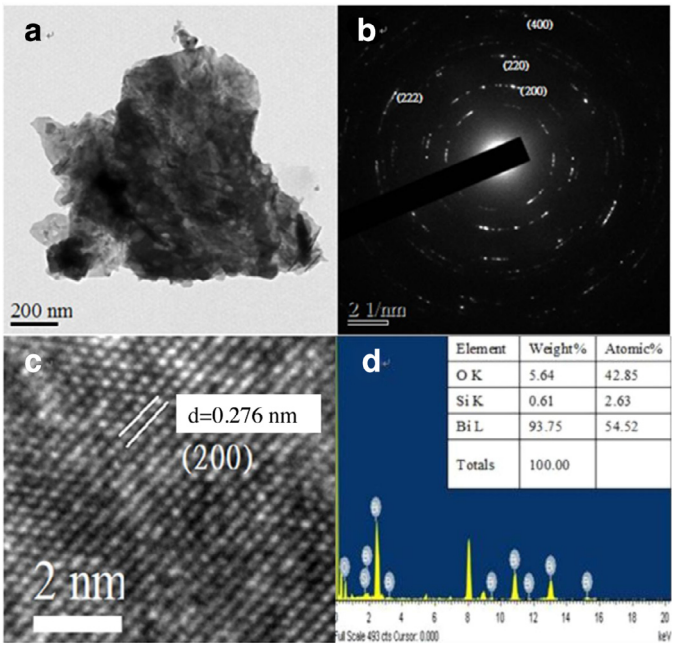

Fig. 3. (a) FE-TEM images, (b) SAED, (c) HRTEM images, and (d) EDS of Bi_2SiO_5 prepared by the hydrothermal autoclave method.

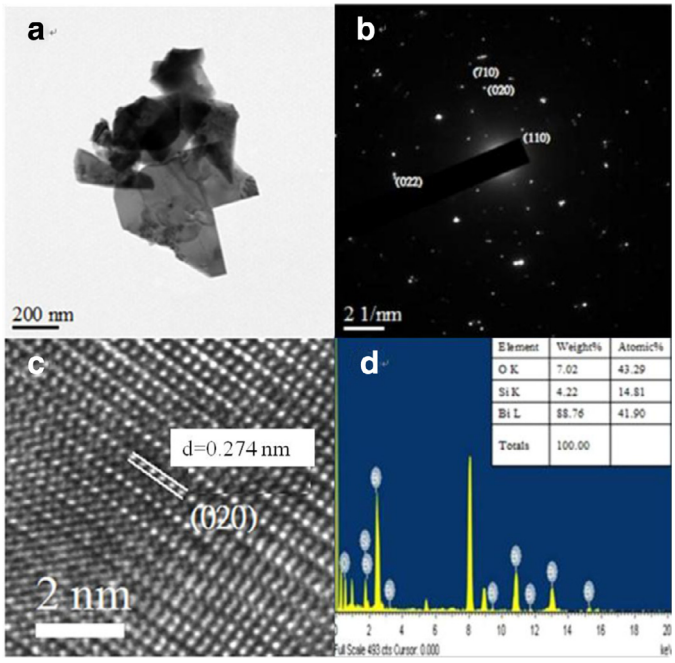

Fig. 4. (a) FE-TEM images, (b) SAED, (c) HRTEM images, and (d) EDS of $Bi_4Si_3O_{12}$ prepared by the hydrothermal autoclave method.

and good stability during rhodamine B photodegradation under visible-light irradiation [20].

Using Bi_2O_3 and SiO_2 as the starting materials, a novel method of melt-cooling processes [21] and molten salt methods in NaCl-Na_2SO_4 flux are applied to prepare pure Bi_2SiO_5 crystals [22]. Chen et al. also synthesized Bi_2SiO_5 with a template-free hydrothermal method, where Bi_2SiO_5 showed high photocatalytic activity toward salicylic acid and benzene under UV-light irradiation [13]. With an emulsion polymerization technique, Police et al. produced porous Bi_2SiO_5 for the isoproturon degradation [23]. Xie et al. synthesized $Bi_4Si_3O_{12}$ with a sol-gel method in which Si $(OC_2H_5)_4$ and Bi $(NO_3)_3$•$5H_2O$ were the precursors and acetic acid was the solvent [24]. $Bi_4Si_3O_{12}$ nanofibers were also synthesized and tested for degrading methylene blue [25]. He and Gu used Bi $(NO_3)_3$ • $5H_2O$ and Si $(OC_2H_5)_4$ as the starting materials for degrading Congo red to prepare $Bi_{12}SiO_{20}$ through a chemical solution decomposition technique [26]. No reports to date have prepared a series of bismuth silicates, $Bi_4Si_3O_{12}$, Bi_2SiO_5, and $Bi_{12}SiO_{20}$ using a template-free hydrothermal method.

Triarylmethane dyes have been used as industrial colorants and antimicrobial agents [27]. However, troubling difficulties have arisen regarding the thyroid peroxidase-catalyzed oxidation of the triarylmethane class of dyes, because the reactions can produce various *N*-de-alkylated primary and secondary aromatic amines with structures similar to those of aromatic amine carcinogens [28]. The photocatalytic degradation of CV, a cationic triarylmethane dye, was studied using several systems to generate active

Table 1
Crystalline phase changes of the as-prepared samples under different hydrothermal conditions. (Bi $[NO_3]_3$ / $NaSiO_3$ = 1/1–3/1, pH = 1–13, temp = 100 °C –250 °C, time = 24 h). (▲ Bi_2SiO_5, ● $Bi_{12}SiO_{20}$, ■ $Bi_4Si_3O_{12}$, ♦ $Bi_6O_6(OH)_3(NO)_3$, △ Bi_2O_3, □ SiO_2).

$Bi_xSi_yO_z$(150°C)					
Bismuth:Silicon molar ratio	pH				
	1	4	7	10	13
1:1	♦	♦	△□	●	●
1:2	♦	♦	△□	●	●
1:3	♦	♦	△□	▲	▲
2:1	♦	♦	△□	▲	▲
2:3	♦	♦	△□	▲	▲
3:1	♦	♦	△□	●	●
3:2	♦	♦	△□	●	●

$Bi_xSi_yO_z$(200°C)					
Bismuth: Silicon molar ratio	pH				
	1	4	7	10	13
1:1	♦	♦	△□	■	■
1:2	♦	♦	△□	■	■
1:3	♦	♦	△□	■	■
2:1	♦	♦	△□	▲	▲
2:3	♦	♦	△□	▲	▲
3:1	♦	♦	△□	▲	▲
3:2	♦	♦	△□	▲	▲

$Bi_xSi_yO_z$(250°C)					
Bismuth: Silicon molar ratio	pH				
	1	4	7	10	13
1:1	♦	♦	△□	▲	▲
1:2	♦	♦	△□	▲	▲
1:3	♦	♦	△□	▲	▲
2:1	♦	♦	△□	▲	▲
2:3	♦	♦	△□	▲	▲
3:1	♦	♦	△□	▲	▲
3:2	♦	♦	△□	▲	▲

species, including Bi_2WO_6 [29], TiO_2 [30], ZnO [31], $SrTiO_3$ [32], BiOX/BiOY(X, Y = Cl, Br, I) [33], $Bi_xAg_yO_z$ [34], $SrFeO_{3-x}$/g-C_3N_4 [35], $PbBiO_2Br$/BiOBr [36], and $BaTiO_3$ [37].

As far as known, there has not been a report in the literature about a series of $Bi_4Si_3O_{12}$, Bi_2SiO_5, and $Bi_{12}SiO_{20}$ syntheses using a hydrothermal method. This is therefore the first report mentioning about $Bi_4Si_3O_{12}$, Bi_2SiO_5, and $Bi_{12}SiO_{20}$ being prepared with a controlled and template-free hydrothermal method and characterized by field-emission scanning electron microscope-electron dispersive X-ray spectroscopy (FE–SEM–EDS), X-ray diffraction (XRD), high-resolution X-ray photoelectron spectroscopy (HR–XPS), and diffuse reflectance ultraviolet visible spectroscopy (DRS). We compare and discuss the photocatalytic activities of these three semiconductors, $Bi_4Si_3O_{12}$, Bi_2SiO_5, and $Bi_{12}SiO_{20}$, by degrading CV in aqueous solution under visible-light irradiation.

2. Experimental details

2.1. Materials

Na_2SiO_3 and $NH_4C_2O_4$ (Osaka), Bi $(NO_3)_3$ • $5H_2O$, KI and urea (Katayama), CV dye (TCI), *p*-benzoquinone (Alfa Aesar), ammonium oxalate (Osaka), and isopropanol (Merck) were purchased and used without further purification. Reagent-grade CH_3COONH_4, NaOH, HNO_3, and HPLC-grade methanol were obtained from Merck.

2.2. Instruments and analytical methods

The Brunauer–Emmett–Teller (BET) specific surface areas of the samples (S_{BET}) were measured with an automated system (Micrometrics Gemini) using nitrogen gas as the adsorbate at a liquid temperature. FE–SEM–EDS measurements were carried out using a JEOL JSM-7401F at an acceleration voltage of 15 kV. The Al-Kα radiation was generated at 15 kV. The field-emission transmission electron microscopy (FE–TEM) images, the selected area electron diffraction (SAED) patterns, the HRTEM images, and the EDS data were obtained using a JEOL-2010 with an acceleration voltage of 200 kV. The XRD patterns were recorded on a MAC Science MXP18 equipped with Cu-Kα radiation, operated at 40 kV and 80 mA. HRXPS measurements were carried out using an ULVAC-PHI. Ultraviolet (UV) photoelectron spectroscopy measurements were performed using a ULVAC-PHI XPS, PHI Quantera SXM. Photoluminescence (PL) measurements were carried out on a Hitachi F-7000.

2.3. Synthesis of $Bi_4Si_3O_{12}$, Bi_2SiO_5, and $Bi_{12}SiO_{20}$

By mixing 2 mmol Bi $(NO_3)_3$ • $5H_2O$ and 1 mmol Na_2SiO_3 in a 50 ml flask and adding 30 ml 4 M HNO_3 with continuous stirring, 2 M NaOH was further added dropwise to adjust the pH value. After vigorously stirring for 30 min, the solution was transferred into a 30 ml Teflon-lined autoclave for being heated up to 150 °C–250 °C for 24 h and then naturally cooled to room temperature. The resulted solid precipitate was filtered and washed with deion-

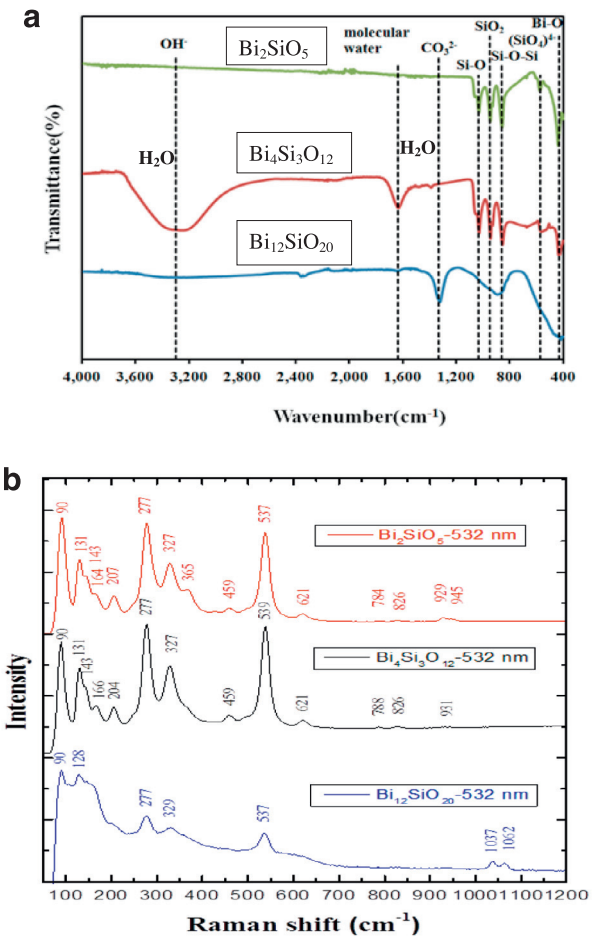

Fig. 5. (a) FT–IR and (b) Raman of the as-prepared Bi_2SiO_5 (B1S1-150-13-24), $Bi_4Si_3O_{12}$ (B1S1-200-13-24), and $Bi_{12}SiO_{20}$ (B1S1-250-13-24).

ized water and methanol to remove any possible ionic species in the solid precipitate. Finally, it was dried at 60 °C overnight.

2.4. Photocatalytic experiments

For the irradiation experiments of CV, an aqueous solution was stirred in a 100-ml flask for an aqueous suspension of 10 ppm, 100 ml CV, which was placed in a Pyrex flask with an amount of catalyst powder. Either HNO_3 or NaOH solution was added for adjusting the pH of the suspension. The adsorption and desorption equilibrium was then examined with a dark experiment. After mixing 10 mg of the photocatalyst into 100 ml CV aqueous solution with a known initial concentration in a 100 ml flask, the mixture was shaken in an orbital shaker (100 rpm) at a constant temperature. Batch sorption experiments were conducted with UV–PDA to determine the absorbance of CV at 580 nm; then the mixture was centrifuged at 3000 rpm in a centrifugation machine. Linear regression was applied to determine the concentration of the solution. Magnetically stirring the suspension in dark for approximately 30 min to establish an adsorption and desorption equilibrium between the CV and the catalyst surface. 15 W Xe arc lamps were then used for the irradiation. The reaction vessel was placed 30 cm from the light source, which was fixed at 0.312 W/cm^2. Within given irradiation time intervals, 5-ml aliquots were collected and centrifuged to remove the catalyst. Eventually, a UV–PDA was used for measuring the supernatant.

Table 2
Physical and chemical properties of $BiSi_xO_y$.

Catalyst code	EDS of atomic ratio (%)			E_g (eV)
	Bi	Si	O	
B1S1-150-13-24	25.63	1.94	72.43	2.69
B1S2-150-13-24	29.26	3.75	66.99	3.35
B1S3-150-13-24	22.70	10.04	67.26	2.85
B2S1-150-13-24	23.37	9.91	66.72	2.58
B2S3-150-13-24	22.70	10.04	67.26	2.63
B3S1-150-13-24	21.39	10.42	68.19	2.58
B3S2-150-13-24	27.32	3.27	69.40	2.55
B1S1-200-13-24	23.09	9.43	67.48	3.44
B1S2-200-13-24	22.70	10.04	67.26	2.66
B1S3-200-13-24	29.32	3.13	67.55	3.30
B2S1-200-13-24	27.32	3.27	69.40	3.30
B2S3-200-13-24	29.26	3.75	66.99	3.51
B3S1-200-13-24	20.90	9.77	69.33	2.53
B3S2-200-13-24	23.37	9.91	66.72	2.66
B1S1-250-13-24	23.39	9.88	66.73	3.55
B1S2-250-13-24	19.84	7.53	72.63	2.58
B1S3-250-13-24	19.81	7.59	72.60	2.35
B2S1-250-13-24	23.37	9.91	66.72	2.58
B2S3-250-13-24	21.84	9.53	68.63	2.61
B3S1-250-13-24	23.37	9.91	66.72	2.58
B3S2-250-13-24	19.84	7.53	72.63	2.58

3. Results and discussion

3.1. Characterization of $Bi_4Si_3O_{12}$, Bi_2SiO_5, and $Bi_{12}SiO_{20}$ composites

3.1.1. Phase structure

Figs. 1 and S1 show the XRD patterns of the as-prepared samples, which clearly present the existence of $Bi_4Si_3O_{12}$ (JCPDS 01-076-1726), Bi_2SiO_5 (JCPDS 01-075-1483), $Bi_{12}SiO_{20}$ (JCPDS 01-080-0627), $Bi_6O_6(OH)_3(NO_3)_3$ (JCPDS 53–1038), Bi_2O_3 (JCPDS 41–1449), and SiO_2 (JCPDS 29–0085) phases. A small amount of impurity phase contamination was noted in almost all samples due to the reactant of non-stiochiometry. Under basic conditions, $Bi_{12}SiO_{20}$ was obtained at pH = 10–13, temp = 150 °C, and molar ratio (Bi/Si) = 1/1, 1/2, 3/1, 3/2; Bi_2SiO_5 was obtained at pH = 10–13, temp = 150 °C, Bi/Si = 1/3, 2/1, 2/3 and pH = 10–13, temp = 200 °C, Bi/Si = 2/1, 2/3, 3/1, 3/2, and pH = 10–13, temp = 250 °C, Bi/Si = 1/1–3/1; and, $Bi_4Si_3O_{12}$ was obtained at pH = 10–13, temp = 200 °C, Bi/Si = 1/1–1/3. Under acidic conditions, Bi_6O_6 $(OH)_3$ $(NO_3)_3$ was obtained at pH = 1–4, temp = 150 °C–250 °C, Bi/Si = 1/1–3/1; and, Bi_2O_3/SiO_2 composites were obtained at pH = 7, temp = 150 °C–250 °C, Bi/Si = 1/1–3/1 in natural conditions. Figs 2–4 show that the $Bi_4Si_3O_{12}$, Bi_2SiO_5, and $Bi_{12}SiO_{20}$ samples consist of layers with different sizes, which is consistent with the TEM observations. Furthermore, the EDS spectrum reveals the composition of Bi, Si, and O in the sample. The HRTEM images appear one set of different lattice images with a d-spacing of 0.289 nm, corresponding to the (321) plane of $Bi_{12}SiO_{20}$, a d-spacing of 0.276 nm, corresponding to the (200) plane of Bi_2SiO_5, and a d-spacing of 0.274 nm, corresponding to the (020) plane of $Bi_4Si_3O_{12}$. This was in agreement with the XRD results. The results suggest that the $Bi_4Si_3O_{12}$, Bi_2SiO_5, and $Bi_{12}SiO_{20}$ phases were synthesized using controlled template-free hydrothermal methods. According to the results summarized in Table 1, the controllable crystal phases of bismuth silicates can be completed by simply changing some growth parameters, including pH, molar ratio (Bi/Si), and temperature.

The FT–IR results are shown in Fig. 5(a). According to previous reports [38,39], the peaks located around 430 cm^{-1}, 570 cm^{-1}, 857 cm^{-1}, 946 cm^{-1}, and 1030 cm^{-1} present the stretching vibration mode of Bi–O bonds, $(SiO_4)^{4-}$ groups, Bi–O–Si bonds, isolated $(SiO_5)^{6-}$ groups, and Si–O bonds, respectively. Raman spec-

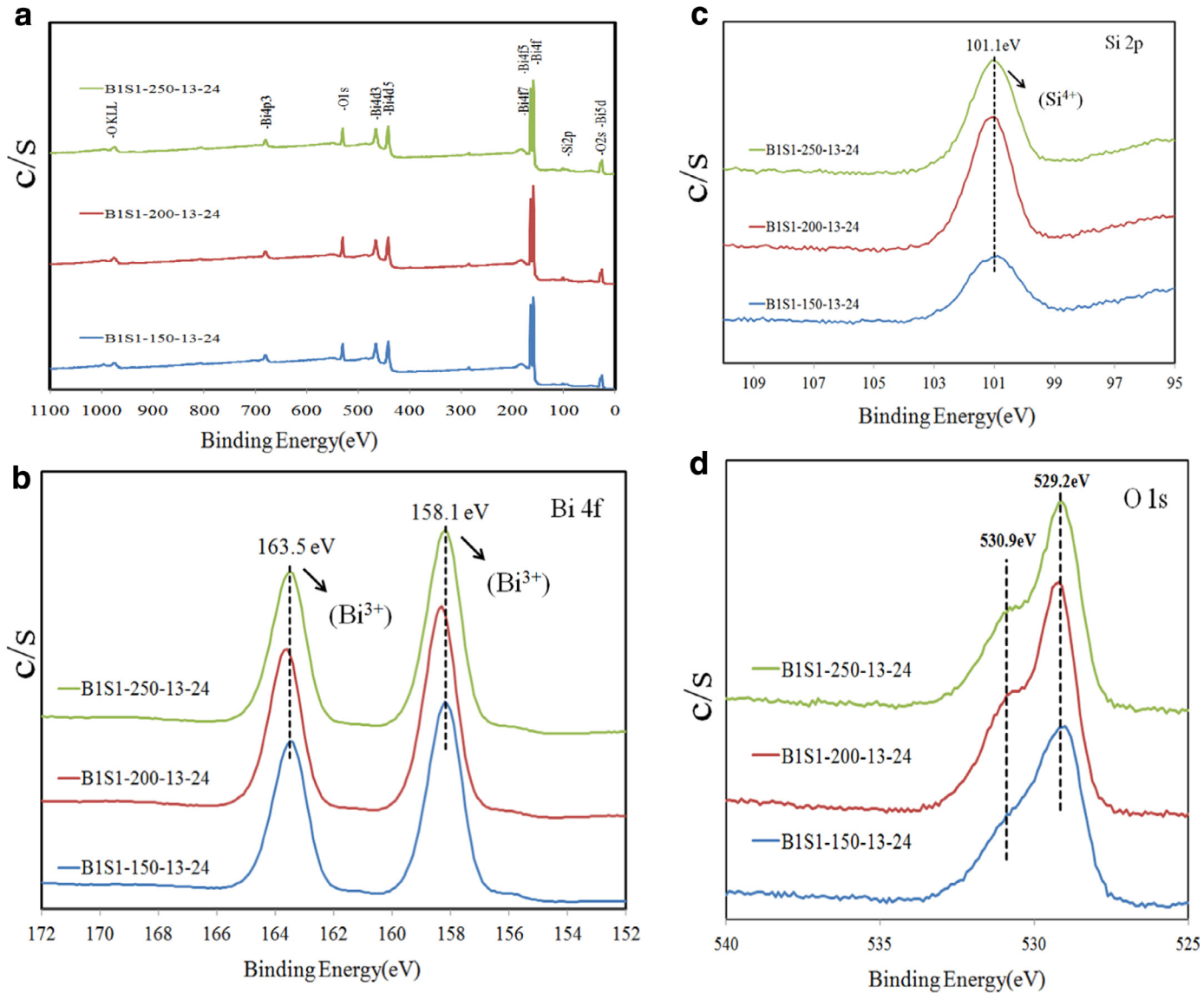

Fig. 6. XPS of the as-prepared $Bi_{12}SiO_{20}$ (B1S1-150-13-24), $Bi_4Si_3O_{12}$ (B1S1-200-13-24), and Bi_2SiO_5 (B1S1-250-13-24).

tra of the bismuth silicates in the frequency range 50–1200 cm^{-1} are shown in Fig. 5(b). The modes in the interval 45–170 cm^{-1} are due to the lattice modes. The internal modes related to Bi–O and SiO_4 tetrahedral appear between 200 and 850 cm^{-1} [40,41]. The peaks located around 90 cm^{-1}, 131 cm^{-1}, 143 cm^{-1}, 207 cm^{-1}, 227 cm^{-1}, 327 cm^{-1}, and 537 cm^{-1} belong to the stretching vibration mode of Bi—O bonds. Other peaks located around 164 cm^{-1}, 459 cm^{-1}, 784 cm^{-1}, and 826 cm^{-1} belong to the stretching vibration modes of Si—O bonds, $(SiO_4)^{4-}$ groups, Bi—O—Si bonds, isolated $(SiO_5)^{6-}$ groups, and Si–O bonds, respectively. In the Raman spectra of $Bi_{12}SiO_{20}$, all the modes of SiO_4 and Bi_3O_4 units are Raman active in the bismuth silicate crystal lattice, and their corresponding Raman peak positions are in excellent agreement with the values in the literature [42,43]. The vibration peak intensity of the SiO_4 tetrahedron is much weaker than that of Bi–O because the tightly bound SiO_4 tetrahedron is surrounded by a “sphere” of 12 heavy bismuth atoms. The crystal structure of Bi_2SiO_5 has previously been reported to be an orthorhombic $Cmc2_1$ at room temperature. The structure is layered, comprising a single layer of one-dimensional silicate chains sandwiched between Bi_2O_2 sheets [44]. Fig. 5(b) shows the Raman spectrum of $Bi_4Si_3O_{12}$ at ambient pressure is in excellent agreement with those in earlier reports [45]. These results are similar to those in the XRD and TEM experiments.

Bi_2SiO_5/g-C_3N_4, with high photocatalytic activity toward CV under visible-light irradiation, is also synthesized in this study by using a template-free hydrothermal method [14]. The formation processes of a series of bismuth silicates were proposed in Eqs. (1)–(4) by Yang et al. [14]. The results demonstrate a series of changes in the compounds prepared under different hydrothermal conditions, described as $Bi_2Si_3O_9 \rightarrow Bi_4Si_3O_{12} \rightarrow Bi_2SiO_5 \rightarrow Bi_{12}SiO_{20}$. By controlling the pH of the hydrothermal reaction, the following compositions of bismuth silicates are obtained.

$$2Bi^{3+} + 3SiO_3^{2-;} \rightarrow Bi_2Si_3O_{9(s)} \quad (1)$$

$$2Bi_2Si_3O_{9(s)} + 6OH^- \rightarrow Bi_4Si_3O_{12(s)} + 3SiO_3^{2-} + 3H_2O \quad (2)$$

$$Bi_4Si_3O_{12(s)} + 2OH^- \rightarrow 2Bi_2SiO_{5(s)} + SiO_3^{2-} + H_2O \quad (3)$$

$$6Bi_2SiO_{5(s)} + 10OH^- \rightarrow Bi_{12}SiO_{20} + 5SiO_3^{2-} + 5H_2O \quad (4)$$

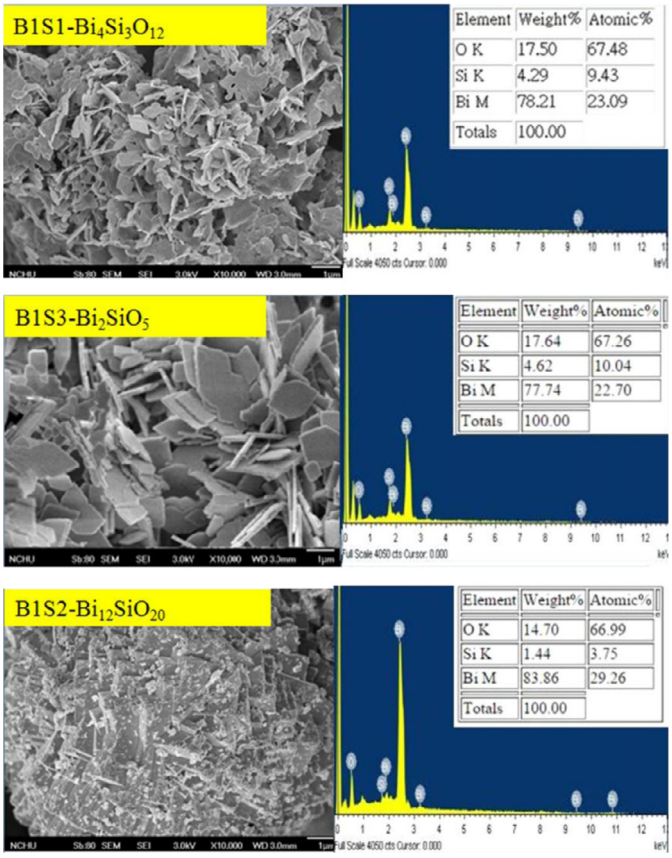

Fig. 7. FE–SEM–EDS of the as-prepared $Bi_{12}SiO_{20}$, $Bi_4Si_3O_{12}$, and Bi_2SiO_5.

3.1.2. XPS analysis

Fig. 6 displays the Bi 4f, Si 2p, and O 1 s XPS spectra of $Bi_4Si_3O_{12}$, Bi_2SiO_5, and $Bi_{12}SiO_{20}$, respectively. The transition peaks involving in the Bi 4f, Si 2p, and O 1 s orbits shows the respective compositions of Bi, Si, and O of the catalysts. The characteristic binding-energy value for Bi $4f_{7/2}$, 158.1 eV, (Fig. 6(b)) shows a trivalent oxidation state for bismuth. Huang et al. [46] also published a similar binding energy for Bi $4f_{7/2}$. In Fig. 6(c), the binding energy for Si $2p_{3/2}$, 101.0 eV, indicates Si at the tetravalent oxidation state. The asymmetric O 1 s peak, Fig. 6(d), can be split with an XPS peak-fitting program. The peak at 530.9 eV is assigned to the external −OH group or the water molecules adsorbed on the surface, while the other O 1 s peak at 529.2 eV corresponds to lattice oxygen atoms in bismuth silicates [36,47].

3.1.3. Morphological structure and composition

Controlled solution chemical synthetic methods are efficient in producing inorganic nanocrystals with a wide variety of composition, size, and shape, in addition to unique electronic, magnetic and optical emission properties [48–50]. Yang et al. reported that controlled growth of nanocrystals was produced by self-seeded nucleation with preferential thermodynamic stability. The intermediate reactants underwent in situ phase transformation to form the final products. The growth followed by irreversible phase transformation leading to the complete separation of nucleation and growth, thereby allowing size tuning of the final nanocrystals [50].

When the formation of crystalline bismuth silicate powders under hydrothermal conditions was complete, the resulting particles grew through Ostwald ripening, which was the final stage of a first-order phase transformation process. The first stage of nucleation was the result of a high degree of super-saturation of the solution; the second stage of particle growth results from the deposition of solute, which led to a decrease in super-saturation and yields a distribution of particles of various sizes. Ostwald ripening or particle coarsening occurred when the super-saturation became very light. The driving force behind coarsening was a reduction in the total surface free energy resulting from the growth of larger particles at the expense of the dissolution of smaller ones [51–53].

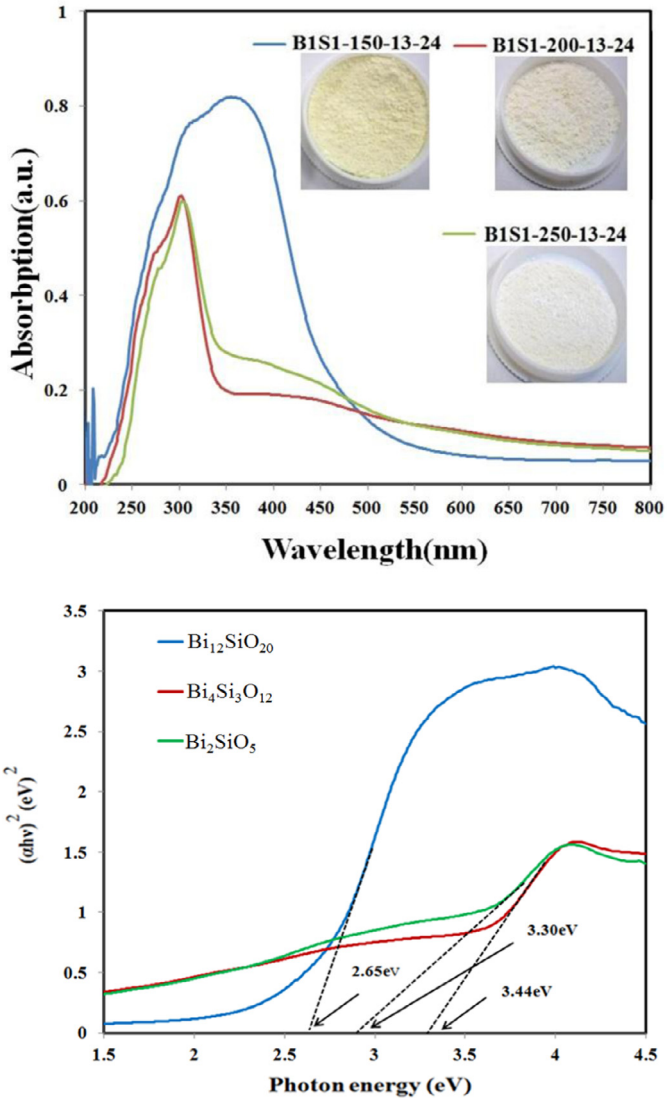

Fig. 8. DRS patterns of the as-prepared $Bi_{12}SiO_{20}$, $Bi_4Si_3O_{12}$, and Bi_2SiO_5.

Fig. 7 shows the FE–SEM images of $Bi_4Si_3O_{12}$, Bi_2SiO_5, and $Bi_{12}SiO_{20}$ at high magnification. The $Bi_4Si_3O_{12}$, Bi_2SiO_5, and $Bi_{12}SiO_{20}$ samples show thin irregular nano-sheet, square-plate, and stacked-square-plate morphologies, respectively. The SEM–EDS and TEM–EDS results demonstrate that bismuth, silicon, and oxygen are the main elements of these samples, Figs 2–5 and 7. The composition of the as-prepared samples contains bismuth, silicon, and oxygen, Table 2. Such results indicate that $Bi_4Si_3O_{12}$, Bi_2SiO_5, and $Bi_{12}SiO_{20}$ could be selectively synthesized through a controlled hydrothermal method.

3.1.4. Optical absorption properties

DR–UV spectra of the samples are shown in Fig. 8. Police et al. reported that bismuth modified silica samples showed an intense band centered at 240 nm, and this implied the presence of a ligand to metal charge transfer involving isolated Bi atoms (Si-O-Bi-O-Si) in the structure of silica [54]. The DR–UV spectra for a silica and

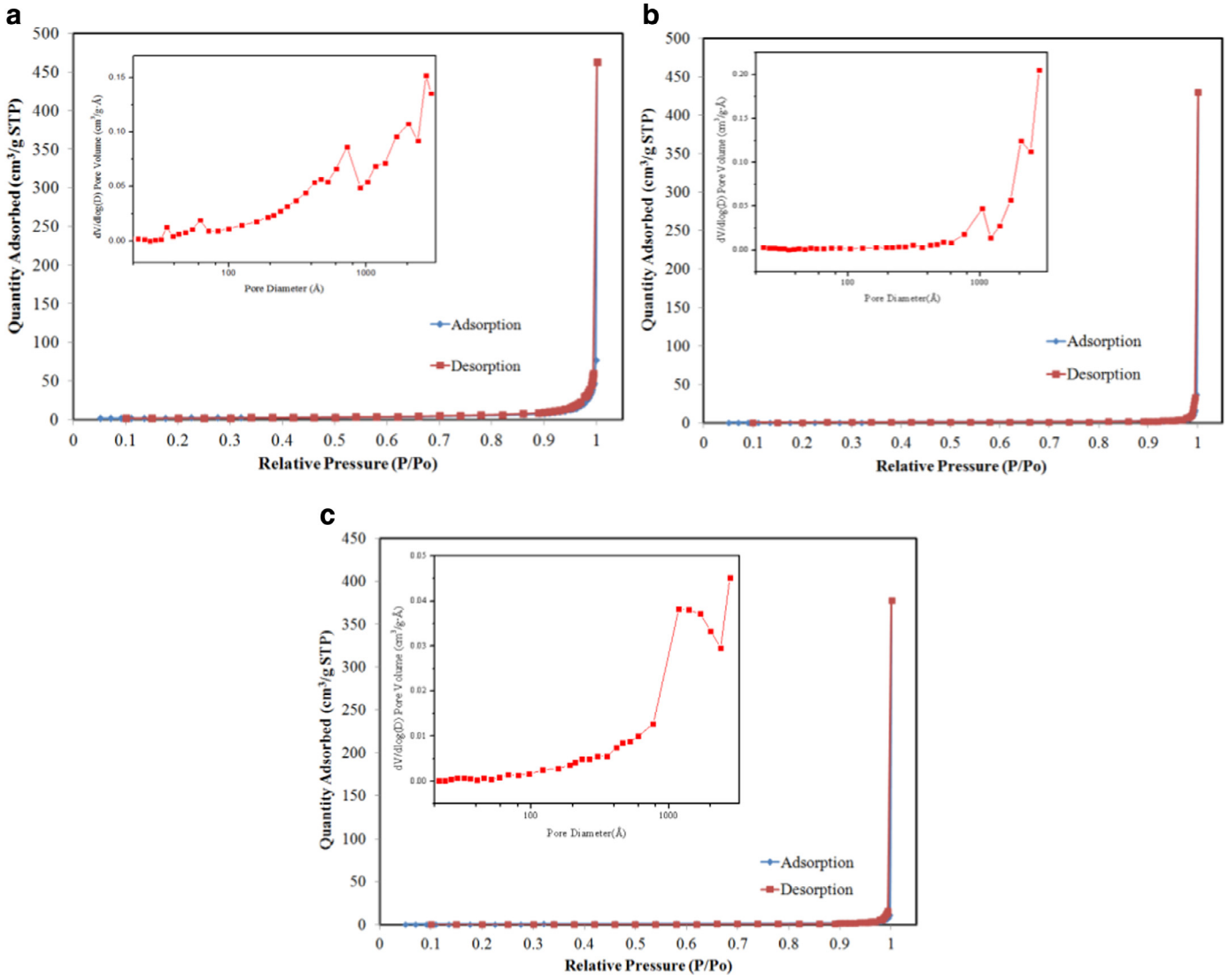

Fig. 9. N_2 adsorption-desorption isotherms, pore size distributions, specific surface areas, pore volumes, and pore diameters of (a) Bi_2SiO_5, (b) $Bi_4Si_3O_{12}$, and (c) $Bi_{12}SiO_{20}$.

bismuth oxide mixture show a large absorption at ca. 400 nm [55]. All the bismuth silicate show an intense band centered at 400 nm, and this bond infers the presence of $[Bi_2O_2]^{2+}$ slabs with the silicate in the structure of bismuth silicate. All the bismuth silicate shows an intense band centered at 275 nm, and this infers the presence of a ligand to metal charge transfer involving isolated Bi atoms (Si-O-Bi-O-Si) in the structure of bismuth silicate. In addition to this band, a band centered at 310 nm is found for the bismuth silicate, and it indicates the existence of another kind of bismuth species at high bismuth contents, which may be assigned to the formation of polymeric bismuth species (Bi-O-Bi). It is in consistent with the results obtained by Raman, IR, and XRD spectra [54,56]. From the above results, it can be concluded that at higher bismuth contents, the bismuth oxides are well reacted into the structure of silicate and exist as $Bi_4Si_3O_{12}$ and Bi_2SiO_5, whereas, at higher bismuth contents, they exist as $Bi_{12}SiO_{20}$. The results indicate that there is the formation of bismuth silicate in the samples.

Fig. 8 shows the DR–UV results for $Bi_4Si_3O_{12}$, Bi_2SiO_5, and $Bi_{12}SiO_{20}$, whose absorption edges are at approximately 360.5, 375.8, and 467.9 nm, respectively. $Bi_4Si_3O_{12}$, Bi_2SiO_5, and $Bi_{12}SiO_{20}$ absorb merely a small amount of visible light. The E_g value of $Bi_4Si_3O_{12}$, Bi_2SiO_5, and $Bi_{12}SiO_{20}$, as 3.44, 3.30, and 2.65 eV respectively, is determined by a plot of $(\alpha h\nu)^{1/2}$ vs energy ($h\nu$), which is consistent with the reported results [25,36,57,58]. Moreover, the energy gaps of the as-prepared samples are listed in Table 2 in the 2.35–3.55 eV range.

3.1.5. Adsorption-desorption isotherm

Fig. 9 shows the nitrogen adsorption-desorption isotherm curves of Bi_2SiO_5, $Bi_4Si_3O_{12}$, and $Bi_{12}SiO_{20}$. The isotherms of Bi_2SiO_5, $Bi_4Si_3O_{12}$, and $Bi_{12}SiO_{20}$ are close to Type IV with a hysteresis loop at a highly relative pressure between 0.6 and 1.0 [36,59]. The shape of the hysteresis loop is close to Type H3, suggesting that the existence of slit-like pores is generally formed by the aggregation of plate-like particles. Such a result is consistent with the self-assembled nanoplate-like morphology of the samples as well as the image results of SEM and TEM, revealing the formation of hierarchical architectures resulted from self-assembled nanosheets or nanoplates.

The BET of Bi_2SiO_5, $Bi_4Si_3O_{12}$, and $Bi_{12}SiO_{20}$ were about 20.78, 2.76, 1.54 m^2g^{-1}, respectively. This nanosheet and nanoplate structure could provide efficient transport paths for reactants and more active sites for the photocatalytic reaction. The structure was also favorable to efficient photo-energy harvesting and intro-

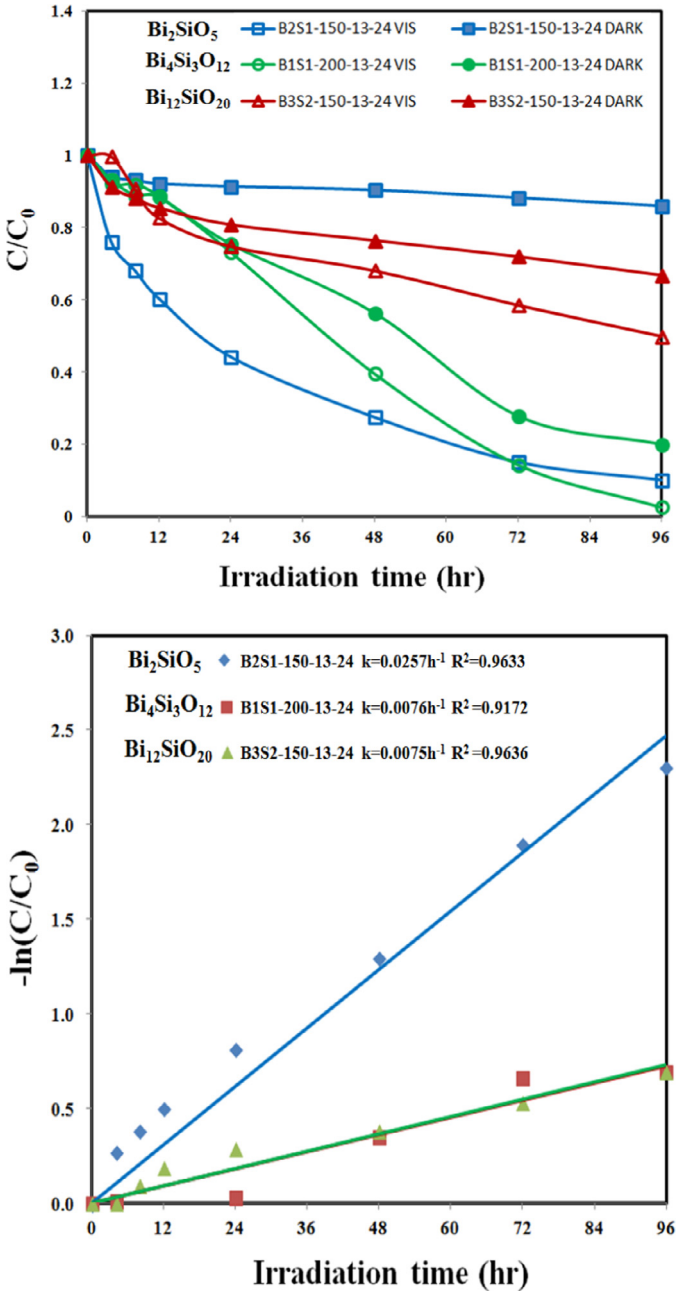

Fig. 10. Photodegradation of CV as a function of irradiation time for $Bi_{12}SiO_{20}$, $Bi_4Si_3O_{12}$, and Bi_2SiO_5 samples.

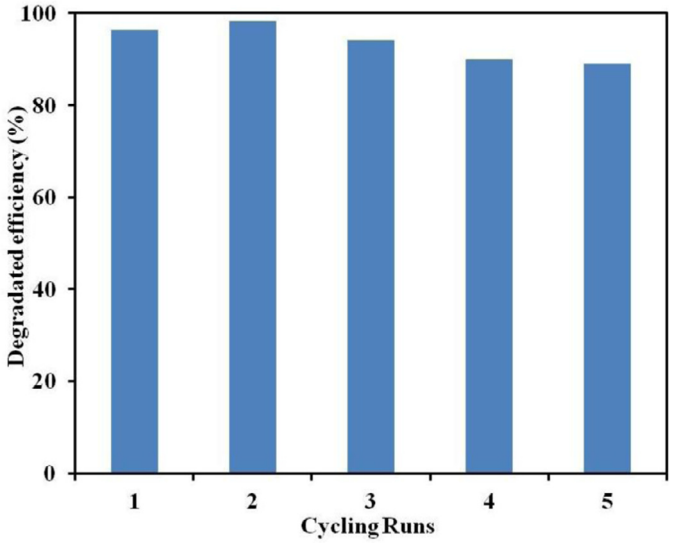

Fig. 11. Cycling runs in the photocatalytic degradation of CV in the presence of Bi_2SiO_5.

Table 3
Pseudo-first-order rate constants for the degradation of CV with $Bi_{12}SiO_{20}$, $Bi_4Si_3O_{12}$, and Bi_2SiO_5 photocatalysts under visible-light irradiation.

Bi_2SiO_5	$k(h^{-1})$	R^2
B1S3-150-13-24	0.0101	0.9964
B2S1-150-13-24	0.0257	0.9633
B2S3-150-13-24	0.0152	0.9924
B2S1-200-13-24	0.0213	0.9629
B2S3-200-13-24	0.0238	0.9626
B3S1-200-13-24	0.0148	0.9223
B3S2-200-13-24	0.0163	0.9468
B1S1-250-13-24	0.0213	0.9575
B1S2-250-13-24	0.0238	0.9723
B1S3-250-13-24	0.0148	0.9646
B2S1-250-13-24	0.0163	0.9569
B2S3-250-13-24	0.0163	0.9964
B3S1-250-13-24	0.0163	0.9949
B3S2-250-13-24	0.0163	0.9738
$Bi_4Si_3O_{12}$	$k(h^{-1})$	R^2
B1S1-200-13-24	0.0076	0.9172
B1S2-200-13-24	0.0057	0.9273
B1S3-200-13-24	0.0044	0.9274
$Bi_{12}SiO_{20}$	$k(h^{-1})$	R^2
B1S1-150-13-24	0.0025	0.9188
B1S2-150-13-24	0.0054	0.9671
B3S1-150-13-24	0.0074	0.9787
B3S2-150-13-24	0.0075	0.9816

ducing the separation of electron-hole pairs, thus promoting the photocatalytic activities. The pore volumes and sizes of Bi_2SiO_5, $Bi_4Si_3O_{12}$, and $Bi_{12}SiO_{20}$ were distributed to 0.12, 0.025, 0.012 cm^3 g^{-1} and 22.3, 30.23, 37.6 nm, respectively. A greater specific surface area and pore volume of photocatalyst could supply more surface active sites and make reactants transport easier, leading to an enhancement of the photocatalytic performance [60]. Bi_2SiO_5 had larger BET and pore volume. Thus, the large BET and pore volume of Bi_2SiO_5 might play a role in enhancing the photocatalytic activity. These nanosheet and nanoplate structures could provide efficient transport paths for reactants and more active sites for the photocatalytic reaction. The structures were also favorable to efficient photo-energy harvesting and introducing the separation of electron-hole pairs, thus promoting the photocatalytic activity.

3.2. Photocatalytic activity

The degradation efficiency, being a function of reaction time, is illustrated in Fig. 10(a). After 15 W Xe light irradiation for 96 h, $Bi_4Si_3O_{12}$, Bi_2SiO_5, and $Bi_{12}SiO_{20}$ exhibited superior photocatalytic performance, with the CV removal efficiencies of up to 99%, 90%, and 80%, respectively. To explain the reaction kinetics of CV degradation, the apparent pseudo-first-order model [61] expressed by the equation $\ln(C_o/C) = kt$ was applied to the experiments. By the first-order linear fit of the data shown in Fig. 10(b) and Table 3, the k values of Bi_2SiO_5, $Bi_4Si_3O_{12}$, and $Bi_{12}SiO_{20}$ were obtained as maximum degradation rates of 2.57×10^{-2} h^{-1}, 7.6×10^{-3} h^{-1}, and 7.5×10^{-3} h^{-1}, respectively, using the first-order linear fit

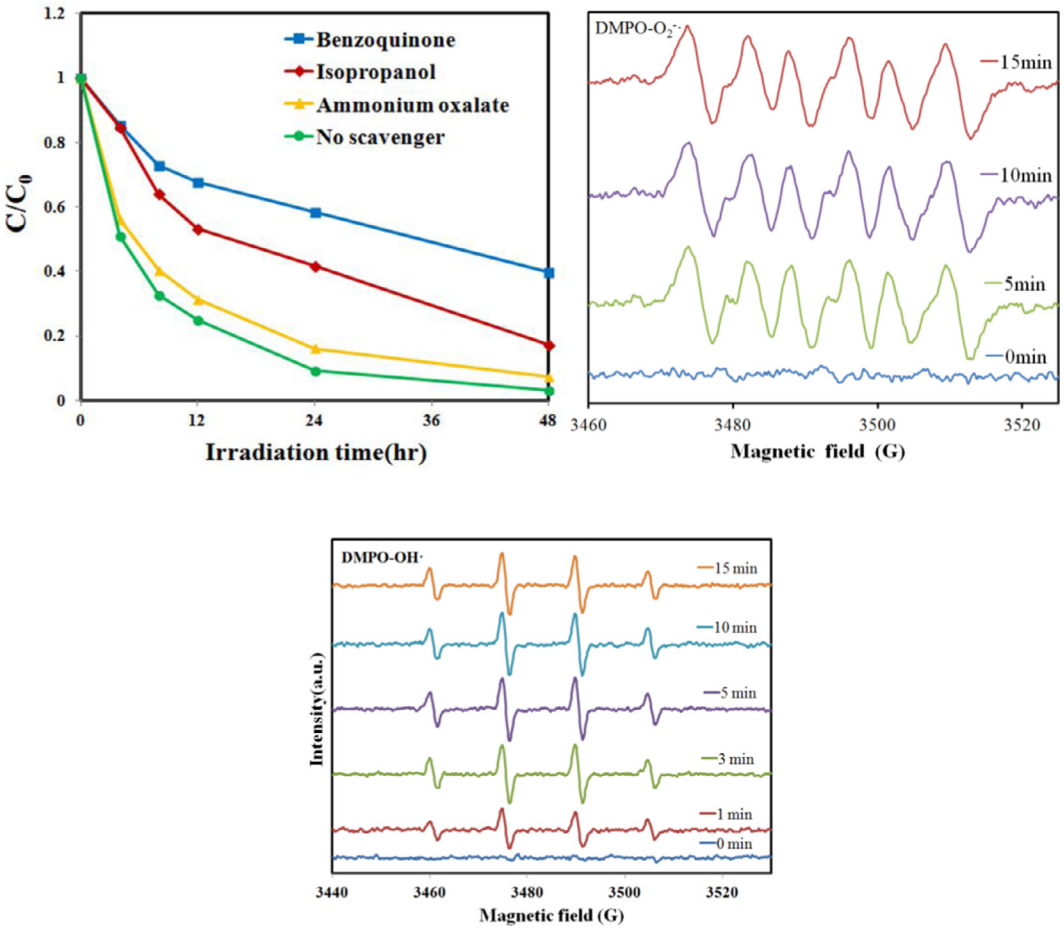

Fig. 12. (a) Trapping experiment of active species and (b) (c) EPR spectra in the methanol dispersion for DMPO–$O_2^{-\bullet}$ and DMPO-$^\bullet$OH during the photocatalytic reaction using Bi_2SiO_5.

of the data in this study. A comparison of rate constants among different photocatalysts is shown in Table 3, and the order appears Bi_2SiO_5 > $Bi_4Si_3O_{12}$ > $Bi_{12}SiO_{20}$. Hu et al. reported that the photocatalytic activities of the as-prepared $Bi_4Si_3O_{12}$ samples were evaluated firstly by the degradation of phenol and Rohdamine B [62]. It showed the concentration changes of phenol at 269 nm as a function of irradiation time during the degradation process in aqueous solution in the presence of $Bi_4Si_3O_{12}$ samples. Obviously, the 98.5% degradation was observed using $Bi_4Si_3O_{12}$ sample after 350 W Xe light irradiation for 180 min, which demonstrated the as-prepared $Bi_4Si_3O_{12}$ photocatalysts exhibiting higher photocatalytic performance.

The durability of Bi_2SiO_5 was evaluated by recycling the used catalyst. After each cycle, the catalyst was collected by centrifugation. No apparent loss was observed in the photocatalytic activity when CV was removed in the 3rd cycle; even during the fifth run, the decline in the photocatalytic activity was 4.7% (Fig. 11). The used Bi_2SiO_5 was also examined by XRD, and no detectable difference was observed between the as-prepared and the used samples; hence, Bi_2SiO_5 had good photostability.

3.3. Photodegradation of CV

In the experiments, CV degradation induced by photolysis under visible light cannot be observed in a blank experiment, as CV is a structure-stable dye, that the decomposition by the photolysis mechanism is negligible. Researchers have reported that various primary active species, such as $O_2^{-\bullet}$, HO$^\bullet$, h^+, H$^\bullet$ and $^1O_2$, can be formated during photodegradation reactions in UV–Vis/semiconductor systems [63,64]. The generation of $O_2^{-\bullet}$ could inhibit the recombination of photoinduced charge carriers as well as benefit the de-chlorination of chlorinated phenol derivatives. The hydroxyl radical HO$^\bullet$ might only be formatted through the route of $e^- \rightarrow O_2^{-\bullet} \rightarrow H_2O_2 \rightarrow {}^\bullet OH$. Furthermore, $^\bullet$OH radicals are formatted by multistep reduction of $O_2^{-\bullet}$ in the system [65]. According to earlier studies [36,66], the photocatalytic process is mainly governed by $O_2^{-\bullet}$, rather than $^\bullet$OH, e^- or h^+; photodegrading CV by BiO_mX_n/BiO_pX_q (X, Y = Cl, Br, I) under visible light, on the other hand, was dominated by $O_2^{-\bullet}$ oxidation, where $O_2^{-\bullet}$ was the main active species and $^\bullet$OH and h^+ were the minor active species [65,67]. Fan et al. revealed [68] that Pt-TiO_2 gathered fewer negative species on catalyst surfaces, which deteriorated reaction rates, than pure TiO_2 did in an acidic environment. The $^\bullet$OH radical was subsequently produced. On the basis of the references presented in previous sections, the probability of forming $^\bullet$OH is proposed to be much lower than that of forming $O_2^{-\bullet}$; however, $^\bullet$OH, being an extremely strong and nonselective oxidant, could lead to the partial or complete mineralization of several organic chemicals.

A series of quenchers were introduced to scavenge the relevant active species in order to evaluate the effect of the active species during the photocatalytic reaction. $O_2^{\bullet -}$, $^\bullet$OH, and h^+ were studied by adding 1.0 mM benzoquinone (BQ, a quencher of $O_2^{\bullet -}$) [69], 1.0 mM isopropanol (IPA, a quencher of $^\bullet$OH) [70], and 1.0 mM ammonium oxalate (AO, a quencher of h^+) [71], respectively. The method was similar to the former photocatalytic activity test.

In order to evaluate the effect of the active species during the photocatalytic processes, a series of quenchers were used for scavenging the relevant active species. As shown in

Fig. 12, the photocatalytic degradation of CV was slightly affected by the addition of AO, while the degradation efficiency of BQ and IPA quenching decreased evidently compared with that of no-quenching, indicating that h^+ was the minor active species, whereas $O_2^{\bullet-}$ and $^{\bullet}OH$ were the major active species in the processes of photocatalytic degradation for CV.

In order to re-evaluate the effect of the active species during the photocatalytic reaction, EPR measurement was used for scavenging the relevant active species. From Fig. 12, not only the six characteristic peaks of the DMPO–$O_2^{-\bullet}$ adducts are observed, but also the four characteristic peaks of DMPO-$^{\bullet}OH$ adducts (1:2:2:1 quartet pattern) are observed under visible light irradiated Bi_2SiO_5 dispersion. Fig. 12 shows that no EPR signal is observed when the reaction is performed in the dark, while the signals with intensity corresponding to the characteristic peak of DMPO-$^{\bullet}OH$ and DMPO–$O_2^{-\bullet}$ adducts [72] are observed during the reaction process under visible light irradiation, and the intensity gradually increases with the prolonged reaction time, suggesting that $O_2^{\bullet-}$ and $^{\bullet}OH$ as active species are formed in the presence of Bi_2SiO_5 and oxygen under visible light irradiation. Therefore, the quenching effects of different scavengers and EPR display that the reactive $O_2^{\bullet-}$ and $^{\bullet}OH$ plays the major role and h^+ play the minor role in the CV of the photocatalytic degradation.

In general, three possible reaction pathways are assumed to possibly be involved in the photodegradation of organisms by a photocatalyst, namely (i) photocatalysis, (ii) photolysis, and (iii) dye photosensitization [73]. In the photolysis process, a $^1O_2$, acting as an oxidant for the photolysis of the organism, is produced by directly reacting a photoinduced electron on the induced organism with O_2 [63]. This indicates that, aside from the degradation of CV by the routes of photocatalytic and photosensitized processes, another type of photocatalytic route accounts for the enhanced photocatalytic activity. Both the photosensitized and photocatalytic processes proceed concurrently. However, in photosensitized and photocatalytic processes, $O_2^{\bullet-}$ radicals are generated by the reaction of photogenerated and photosensitized electrons with oxygen gas on the photocatalyst surface, while $^{\bullet}OH$ radicals are subsequently produced by the reactions of $O_2^{\bullet-}$ radicals with H^+ ions and h^+ holes with OH^- ions (or H_2O). These cycles would continue when the system is exposed to visible-light irradiation [68]. After several cycles of photo-oxidation, the CV degradation with the produced oxidant species can be expressed by Eqs. (5) and (6).

$$CV + O_2^{-\bullet}/OH^{\bullet} \rightarrow \text{decomposed compounds} \quad (5)$$

$$CV+\bullet + O2-\bullet/OH\bullet \rightarrow \text{decomposed compounds} \quad (6)$$

In a visible-light-driven semiconductor system, it proves that hydroxylated compounds would cause the photocatalytic degradation of CV [65,67]. Earlier reports [37,68] indicated that *N*-demethylation processes were preceded by the generation of a nitrogen-centered radical, and the destruction of the dye chromophore structure was preceded by the formation of a carbon-centered radical in the photocatalytic degradation of CV dye under UV or visible-light irradiation. Some notions regarding the applications of the reaction mechanisms for photocatalytic processes proposed in this study to the degradation of dyes should be offered.

4. Conclusions

The composition and morphology of bismuth silicates can be controlled by adjusting some growth parameters, including reaction pH and temperature. Three crystalline substances, $Bi_4Si_3O_{12}$, Bi_2SiO_5, and $Bi_{12}SiO_{20}$, were prepared from the reaction of Na_2SiO_3 and $Bi(NO_3)_3 \bullet 5H_2O$ in alkaline aqueous solution at 150 °C–250 °C for 24 h, whereas conventional synthesis necessitates operational temperatures above 650 °C. The UV–Vis spectra demonstrate the three materials are indirect semiconductors with optical bandgaps of 2.65, 3.30, and 3.44 eV, respectively. The photocatalytic efficiency of the powder suspension was evaluated by measuring the CV concentrations under visible-light irradiation. The order of rate constants shows Bi_2SiO_5 > $Bi_4Si_3O_{12}$ > $Bi_{12}SiO_{20}$. This work is useful for the synthesis of bismuth silicates and the photocatalytic degradation of CV. This will have future applications in the control of environmental pollution.

Acknowledgments

This research was supported by the Ministry of Science and Technology of the Republic of China (MOST-104-2113-M-142-001).

Supplementary materials

Supplementary material associated with this article can be found, in the online version, at doi:10.1016/j.jtice.2017.05.021.

References

[1] Kubacka A, Fernández-García M, Colón G. Advanced nanoarchitectures for solar photocatalytic applications. Chem Rev 2012;112:1555–614.
[2] Cheng H, Huang B, Dai Y. Engineering BiOX (X = Cl, Br, I) nanostructures for highly efficient photocatalytic applications. Nanoscale 2014;6:2009–26.
[3] Ye L, Chen J, Tian L, Liu J, Penga T, Deng K, et al. BiOI thin film via chemical vapor transport: photocatalytic activity, durability, selectivity and mechanism. Appl Catal B: Environ 2013;130–131 1–7.
[4] Pu Y, Li Y, Huang Y, Kim SI, Cai P, Seo HJ. Visible light-induced degradation of methylene blue by photocatalyst of bismuth layered Bi_7VO_{13} nanoparticles. Mater Lett 2015;141:73–5.
[5] Lu Y, Chen L, Huang Y, Cheng H, Kim SI, Seo HJ. Optical properties and visible light-driven photocatalytic activity of $Bi_{11}VO_{19}$ nanoparticles with δ-Bi_2O_3-structure. J Alloys Comp 2015;640:226–32.
[6] Chen Z, Jiang H, Jin W, Shi C. Enhanced photocatalytic performance over $Bi_4Ti_3O_{12}$ nanosheets with controllable size and exposed (0 0 1) facets for Rhodamine B degradation. Appl Catal B: Environ 2016;180:698–706.
[7] Liao YH, Wang JX, Lin JS, Chung WH, Lin WY, Chen CC. Synthesis photocatalytic activities and degradation mechanism of Bi_2WO_6 toward crystal violet dye. Catal Today 2011;174:148–59.
[8] Seabold JA, Choi KS. Efficient and stable photo-oxidation of water by a bismuth vanadate photoanode coupled with an iron oxyhydroxide oxygen evolution catalyst. J Am Chem Soc 2012;134:2186–92.
[9] Xu L, Wan Y, Xie H, Huang Y, Qiao X, Qin L, et al. On structure, optical properties and photodegradated ability of aurivillius-type Bi_3TiNbO_9 nanoparticles. J Am Ceram Soc 2016;99:3964–72.
[10] Wei W, Dai Y, Huang BB. First-principles characterization of Bi-based photocatalysts: $Bi_{12}TiO_{20}$, $Bi_2Ti_2O_7$, and $Bi_4Ti_3O_{12}$. J Phys Chem C 2009;113:5658–63.
[11] Fei Y, Fan S, Sun R, Ishii M. Study on phase diagram of Bi_2O_3-SiO_2 system for Bridgman growth of $Bi_4Si_3O_{12}$ single crystal. Prog Cryst Growth Charact 2000;40:183–8.
[12] Corsmit G, Van Driel MA, Elsenaar RJ. Thermal analysis of bismuth germanate compounds. J Cryst Growth 1986;75:551–5.
[13] Chen R, Bi J, Wu L, Wang W, Li Z, Fu X. Template-free hydrothermal synthesis and photocatalytic performances of novel, Bi_2SiO_5 nanosheets. Inorg Chem 2009;48:9072–6.
[14] Yang CT, Lee WW, Lin HP, Dai YM, Chi HT, Chen CC. A novel heterojunction photocatalyst, Bi_2SiO_5/g-C_3N_4: synthesis, characterization, photocatalytic activity, and mechanism. RSC Adv 2016;6:40664–75.
[15] Wintermantel M, Biaggio I. Temperature-dependent electron mobility and large polaron interpretation in $Bi_{12}SiO_{20}$. Phys Rev B 2003;67:165108.
[16] Xu H, Sun Q, An Z, Wei Y, Liu X. Electroluminescence from europium(III) complexes. Coord Chem Rev 2015;293–294:228–49.
[17] Dong H, Sun LD, Yan CH. Energy transfer in lanthanide upconversion studies for extended optical applications. Chem Soc Rev 2015;44:1608–34.
[18] Wang X, Liu Q, Bu Y, Liu CS, Liu T, Yan X. Optical temperature sensing of rare-earth ion doped phosphors. RSC Adv 2015;5:86219–36.
[19] Ye S, Xiao F, Pan YX, Ma YY, Zhang QY. Phosphors in phosphor-converted white light-emitting diodes: Recent advances in materials, techniques and properties. Mater Sci Engin R 2010;71:1–34.
[20] Duan J, Liu Y, Pan X, Zhang Y, Yu J, Nakajim K, Taniguchi H. High photodegradation efficiency of Rhodamine B catalyzed by bismuth silicate nanoparticles. Catal Commun 2013;39:65–9.
[21] Guo HW, Wang XF, Gao DN. A novel method for preparation of pure Bi_2SiO_5 crystals. Mater Lett 2012;67:280–2.
[22] Lu J, Wang X, Wu Y, Xu Y. Synthesis of Bi_2SiO_5 powder by molten salt method. Mater Lett 2012;74:200–2.
[23] Police AKR, Basavaraju S, Valluri DK. Bismuth modified porous silica preparation, characterization and photocatalytic activity evaluation for degradation of isoproturon. J Mater Sci Technol 2013;29:639–46.

[24] Xie H, Jia C, Jiang Y, Wang X. Synthesis of $Bi_4Si_3O_{12}$ powders by a sol-gel method. Mater Chem Phys 2012;133:1003–5.
[25] Batool SS, Hassan S, Imran Z, M Rafiq A, Ahmad M, Rasool K, Chaudhry MM, Hasan MM. The enhancement in photocatalytic activity of bismuth modified silica and bismuth silicate nanofibers. Catal Commun 2014;4:39–42 9.
[26] He C, Gu M. Preparation, characterization and photocatalytic properties of $Bi_{12}SiO_{20}$ powders. Scrip Mater 2006;55:481–4.
[27] Duxbury DF. The photochemistry and photophysics of triphenylmethane dyes in solid and liquid media. Chem Rev 1993;93:381–433.
[28] Cho BP, Yang T, Blankenship LR, Moody JD, Churchwell M, Bebland FA, Culp SJ. Synthesis and characterization of *N*-demethylated metabolites of malachite green and leucomalachite Green. Chem Res Toxicol 2003;16:285–94.
[29] Lee WLW, Lin JS, Chang JL, Chen JY, Cheng MC, Chen CC. Photodegradation of CV over nanocrystalline bismuth tungstate prepared by hydrothermal synthesis. J Mol Catal A: Chem 2012;361–362:80–90.
[30] Chen F, Fang P, Gao Y, Liu Z, Liu Y, Dai Y. Effective removal of high-chroma crystal violet over TiO_2-based nanosheet by adsorption–photocatalytic degradation. Chem Eng J 2012;204–206:107–13.
[31] Ameen S, Akhtar MS, Nazim M, Shin HS. Rapid photocatalytic degradation of crystal violet dye over ZnO flower nanomaterials. Mater Lett 2013;96:228–32.
[32] Huang ST, Lu CS, Chang JL, Huang WS, Chen CC. Hydrothermal synthesis of cubic-$SrTiO_3$: characterization, photocatalytic activities, and degradation pathway. J Taiwan Inst Chem Eng 2014;45:1927–36.
[33] Huang ST, Jiang YR, Chou SY, Dai YM, Chen CC. Synthesis, characterization, photocatalytic activity of visible-light-responsive photocatalysts BiO_xCl_y/BiO_mBr_n by controlled hydrothermal method. J Mol Catal A: Chem 2014;391:105–20.
[34] Yu K, Yang S, Liu C, Chen H, Li H, Sun C, Boyd SA. Degradation of organic dyes via bismuth silver oxide initiated direct oxidation coupled with sodium bismuthate based visible light photocatalysis. Environ Sci Technol 2012;46:7318–26.
[35] Lin HP, Chen CC, Lee WW, Lai YY, Chen JY, Chen YQ, Fu JY. Synthesis of $SrFeO_{3-x}/g\text{-}C_3N_4$ heterojunction with improved visible-light photocatalytic activities in chloramphenicol and crystal violet degradation. RSC Adv 2016;6:2323–36.
[36] Lin HP, Lee WW, Huang ST, Chen LW, Yeh TW, Fu JY, Chen CC. Controlled hydrothermal synthesis of $PbBiO_2Br$/BiOBr heterojunction with enhanced visible–driven-light photocatalytic activities. J Mol Catal A: Chem 2016;417:168–83.
[37] Lee WLW, Chung WH, Huang WS, Lin WC, Lin WY, Jiang YR, Chen CC. Photocatalytic activities of nano-cubic barium titanate by hydrothermal synthesis. J Taiwan Inst Chem Eng 2013;44:660–9.
[38] Feng X, Qi X, Li J, Yang L, Qiu M, Yin J, Lu F, Zhong J. Reparation, structure and photo-catalytic performances of hybrid Bi_2SiO_5 modified Si nanowire arrays. Appl Surf Sci 2011;257:5571–5.
[39] Bordun OM. Vibrational spectra of thin eulytine films. J Appl Spectrosc 1997;64:476–9.
[40] Mihailova B, Gospodinov M, Konstantinov L. Raman spectroscopy study of sillenites. I. Comparison between $Bi_{12}(Si,Mn)O_{20}$ single crystals. J Phys Chem Solids 1999;60:1821–7.
[41] Rao R, Garg AB, Sakuntala T. High pressure stability of bismuth sillenite: a Raman spectroscopic and x-ray diffraction study. J Appl Phys 2010;108:83508.
[42] Han Q, Zhang J, Wang X, Zhu J. Preparing $Bi_{12}SiO_{20}$ crystals at low temperature through nontopotactic solid-state transformation and improving its photocatalytic activity by etching. J Mater Chem A 2015;3:7413–21.
[43] Hu Y, Sinclair DC. Relaxor-like dielectric behavior in stoichiometric sillenite $Bi_{12}SiO_{20}$. Chem Mater 2013;25:48–54.
[44] Taniguchi H, Kuwabara A, Kim J, Kim Y, Moriwake H, Kim S, Hoshiyama T, Koyama T, Mori S, Takata M, Hosono H, Inaguma Y, Itoh M. Asymmetric ion pair catalysis of 6π electrocyclizations: brønsted acid catalyzed enantioselective synthesis of optically active 1,4-dihydropyridazines. Angew Chem Int Ed 2013;52:8088–92.
[45] Ravindran TR, Arora AK, Gopalakrishnan R. Pressure-induced amorphization of bismuth orthosilicate. J Phys: Condens Matter 2002;14:6579–89.
[46] Huang ST, Jiang YR, Chou SY, Dai YM, Chen CC. Synthesis, characterization, photocatalytic activity of visible-light-responsive photocatalysts BiO_xCl_y/BiO_mBr_n by controlled hydrothermal method. J Mol Catal A: Chem 2014;391:105–20.
[47] Jiang YR, Lin HP, Chung WH, Dai YM, Lin WY, Chen CC. Controlled hydrothermal synthesis of BiO_xCl_y/BiO_mI_n composites exhibiting visible-light photocatalytic degradation of crystal violet. J Hazard Mater 2015;283:787–805.
[48] Feng X, Sayle DC, Wang ZL, Paras MS, Santora B, Sutorik AC, Sayle TXT, Yang Y, Ding Y, Wang X, Her YS. Converting ceria polyhedral nanoparticles into single-crystal nanospheres. Science 2006;312:1504–8.
[49] Wang X, Bu Y, Xiao Y, Kan C, Lu D, Yan X. Size and shape modifications, phase transition, and enhanced luminescence of fluoride nanocrystals induced by doping. J Mater Chem C 2013;1:3158–66.
[50] Yang L, Li Y, Yu S, Hao J, Zhong J, Chu PK. Phase transformation and size tuning in controlled-growth of nanocrystals via self-seeded nucleation with preferential thermodynamic stability. Chem Commun 2011;47:12544–6.
[51] Sun W. Particle coarsening. I. Kinetics for reversible dissolution/deposition controlled process. Acta Mater 2005;53:3329–34.
[52] Lencka MM, Riman RF. Thermodynamic modeling of hydrothermal synthesis of ceramic powders. Chem Mater 1993;5:61–70.
[53] Sun W, Pang Y, Li J, Ao W. Particle coarsening. II. Growth kinetics of hydrothermal $BaTiO_3$. Chem Mater 2007;19:1772–9.
[54] Kumar A, Police R, Basavaraju S, Valluri KD, Machiraju S. Bismuth modified porous silica preparation, characterization and photocatalytic activity evaluation for degradation of isoproturon. J Mater Sci Technol 2013;29(7):639–46.
[55] Qian G, Ji D, Lu G, Zhao R, Qi Y, Suo J. Bismuth-containing MCM-41: synthesis, characterization, and catalytic behavior in liquid-phase oxidation of cyclohexane. J Catal 2005;232:378–85.
[56] Qian G, Luo X, Wang J. High bismuth content Bi-MCM-41: synthesis, characterization and investigation on the distribution of bismuth atoms. Microporous Mesoporous Mater 2008;112:632–6.
[57] Liu D, Yao W, Wang J, Liu Y, Zhang M, Zhu Y. Enhanced visible light photocatalytic performance of a novel heterostructured $Bi_4O_5Br_2/Bi_{24}O_{31}Br_{10}$/ Bi_2SiO_5 photocatalyst. Appl Catal B: Environ 2015;172–173:100–7.
[58] Liu D, Wang J, Zhang M, Liu Y, Zhu Y. A superior photocatalytic performance of a novel Bi_2SiO_5 flower-like microsphere via a phase junction. Nanoscale 2014;6:15222–7.
[59] Lin L, Yuan S, Chen J, Wang L, Wan J, Lu X. Treatment of chloramphenicol-contaminated soil by microwave radiation. Chemosphere 2010;78:66–71.
[60] Yu JG, Su YR, Cheng B. Template-free fabrication and enhanced photocatalytic activity of hierarchically macro/mesoporpous titania. Adv Funct Mater 2007;17:1984–90.
[61] Chatzitakis A, Berberidou C, Paspaltsis I, Kyriakou G, Sklaviadis T, Poulios I. Photocatalytic degradation and drug activity reduction of Chloramphenicol. Water Res 2008;42:386–94.
[62] Zhang P, Hu J, Li J. Controllable morphology and photocatalytic performance of bismuth silicate nanobelts/nanosheets. RSC Adv 2011;1:1072–7.
[63] Xiao X, Hao R, Liang M, Zuo X, Nan J, Li L, Zhang W. One-pot solvothermal synthesis of three-dimensional (3D) BiOI/BiOCl composites with enhanced visible-light photocatalytic activities for the degradation of bisphenol-A. J Hazard Mater 2012;233–234:122–30.
[64] Dimitrijevic NM, Vijayan BK, Poluektov OG, Rajh T, Gray KA, He H, Zapol P. Role of water and carbonates in photocatalytic transformation of CO_2 to CH_4 on titania. J Am Chem Soc 2011;133:3964–71.
[65] Tian Y, Chang B, Lu J, Fu J, Xi F, Dong X. Hydrothermal synthesis of graphitic carbon nitride–Bi_2WO_6 heterojunctions with enhanced visible light photocatalytic activities. ACS Appl Mater Interfaces 2013;5:7079–85.
[66] Cheng H, Hou J, Takeda O, Guo XM, Zhu H. A unique Z-scheme 2D/2D nanosheet heterojunction design to harness charge transfer for photocatalysis. J Mater Chem A 2015;3:11006–13.
[67] Lee WW, Lu CS, Chuang CW, Chen YJ, Fu JY, Siao CW, Chen CC. Synthesis of bismuth oxyiodides and their composites: characterization, photocatalytic activity, and degradation mechanisms. RSC Adv 2015;5:23450–63.
[68] Fan HJ, Lu CS, Lee WLW, Chiou MR, Chen CC. Mechanistic pathways differences between P25-TiO_2 and Pt-TiO_2 mediated CV photodegradation. J Hazard Mater 2011;185:227–35.
[69] Yin MC, Li ZS, Kou JH, Zou ZG. Mechanism investigation of visible light-induced degradation in a heterogeneous TiO_2/eosin Y/rhodamine B system. Environ Sci Technol 2009;43:8361–6.
[70] Zhang LS, Wong KH, Yip HY, Hu C, Yu JC, Chan CY, Wong PK. Effective photocatalytic disinfection of E. coli K-12 using AgBr–Ag–Bi_2WO_6 nanojunction system irradiated by visible light: the role of diffusing hydroxyl radicals. Environ Sci Technol 2010;44:1392–8.
[71] Meng SG, Li DZ, Sun M, Li WJ, Wang JX, Chen J, Fu XZ, Xiao GC. Sonochemical synthesis, characterization and photocatalytic properties of a novel cube-shaped $CaSn(OH)_6$. Catal Commun 2011;12:972–5.
[72] Xiao X, Xing C, He G, Zuo X, Nan J, Wang L. Solvothermal synthesis of novel hierarchical $Bi_4O_5I_2$ nanoflakes with highly visible light photocatalytic performance for the degradation of 4-tert-butylphenol. Appl Catal B: Environ 2014;148–149:154–63.
[73] Nasr C, Vinodgopal K, Fisher L, Hotchandani S, Chattopadhyay AK, Kamat PV. Environmental photochemistry on semiconductor surfaces. Visible light induced degradation of a textile diazo dye, naphthol blue black, on TiO_2 nanoparticles. J Phys Chem 1996;100:8436–42.